# Large-scale density functional theory simulation of inorganic nanotubes: a case study on Imogolite nanotubes

**E. Poli[1], J. D. Elliott[1], N. D. M. Hine[2,3], A. A. Mostofi[4] and G. Teobaldi*[1]**

The high experimental control over inorganic Imogolite-like open-ended nanotubes (Imo-NTs) composition, dimensions and monodispersity together with the potentially huge range of tuneable properties that can be introduced by chemical functionalisation and doping make Imo-NTs appealing substrates for nanotechnology, as artificial ion-channels and in chemical separation. Investigation of Imo-NTs electronic and spectroscopic properties has so far been hampered by the large size of the systems repeat unit (+300 atoms), which pose severe challenges and accuracy-viability compromises for standard plane-wave (fixed atomic basis set) density functional theory (DFT) simulations. These challenges can, however, be met by linear-scaling DFT (LS-DFT) approaches based on *in situ* optimisation of minimal basis sets. Here, we illustrate the applicability of LS-DFT to Imo-NTs by providing structural and electronic characterisation of periodic and finite models of aluminosilicate (AlSi) and methylated-AlSi Imo-NTs. It is shown that adoption of moderate kinetic energy cutoff (1000 eV) and basis set truncation radius (8 Bohr) leads to optimal accuracy-viability compromised for geometrical optimisation of Imo-NTs. These results should be useful for future LS-DFT investigation of Imo-NTs and other AlSi-based functional materials.

**Keywords:** Inorganic Imogolite nanotubes, Linear-scaling density functional theory

## Introduction

Since the discovery of carbon nanotubes (CNTs) by Ijima in 1991,[1] research in the field of nanotubes has grown significantly, driven by the potential of nanostructured one-dimensional hollow materials for innovative applications in electronics, photonics, sensing, chemical storage and separation as well as (photo-)catalysis, biotechnology and nanofluidics.[1–22] In parallel with the realisation of challenges in straightforward control over CNTs preparation, separation and covalent functionalisation,[2–11] interest in inorganic metal-oxide nanotubes has started to grow, with great progress in the controlled synthesis and functionalisation of open-ended Imogolite-like aluminosilicate (AlSi) and aluminogermanate (AlGe) NTs.[23–31]

The AlSi and AlGe NTs are structurally analogous to the naturally occurring hydrous-AlSi imogolite (Imo[32,33]). Its walls consist of a single layer of octahedrally coordinated aluminium hydroxide (gibbsite) with pendant tetrahedral silanol (Si—OH) groups facing the tube cavity (Fig. 1). From a compositional point of view, the only difference between AlSi and AlGe NTs is the substitution of silanol groups with germanol (Ge—OH) groups. The resulting chemical formulae of the unit cells are $(Al_2SiO_7H_4)_N$ and $(Al_2GeO_7H_4)_N$ for AlSi and AlGe tubes, respectively, with $N$ being the number of radially non-equivalent aluminium atoms along the NT circumference, an even number of symmetry reasons.[34]

Over the last few years, the understanding and control of the growth of these materials has progressed noticeably, with the definition of solution-based synthetic routes to single-walled (SW) AlSi and AlGe NTs of controllable radius and length. In addition, the creation of double-walled (DW) AlGe NTs has also been achieved.[34–37] Important advances have been made in the post-synthetic, selective functionalisation of the outer or inner surface of AlSi NTs,[38–40] and in the direct creation of methylated (AlSiMe)[41,42] or aminated (AlSiAm)[43] AlSi NTs derivatives, with methyl ($-CH_3$, Fig. 1) or amine ($-NH_2$) functions in the NT cavity, instead of silanol groups. Further selective amination of the outer surface of AlSiMe NTs by post-synthesis grafting, yielding hybrid AmAlSiMe derivatives, has also been shown to be possible.[39,40] Exploration of the surface properties of these hybrid materials has revealed superior performances for chemical separation,[39–44] and results on their beneficial role as support for (photo)catalysts[45,46] as well as in hybrid nanocomposites[47] have started to appear in the literature.

[1]Stephenson Institute for Renewable Energy and Department of Chemistry, The University of Liverpool, Liverpool L69 7ZF, UK
[2]Theory of Condensed Matter, Cavendish Laboratory, J. J. Thomson Avenue, Cambridge CB3 0HE, UK
[3]Department of Physics, University of Warwick, Coventry CV4 7AL, UK
[4]The Thomas Young Centre for Theory and Simulation of Materials, Imperial College London, London SW7 2AZ, UK

E. Poli and J.D. Elliott contributed equally to this manuscript.

*Corresponding author, email g.teobaldi@liv.ac.uk


DOI 10.1179/1432891715Z.0000000001560

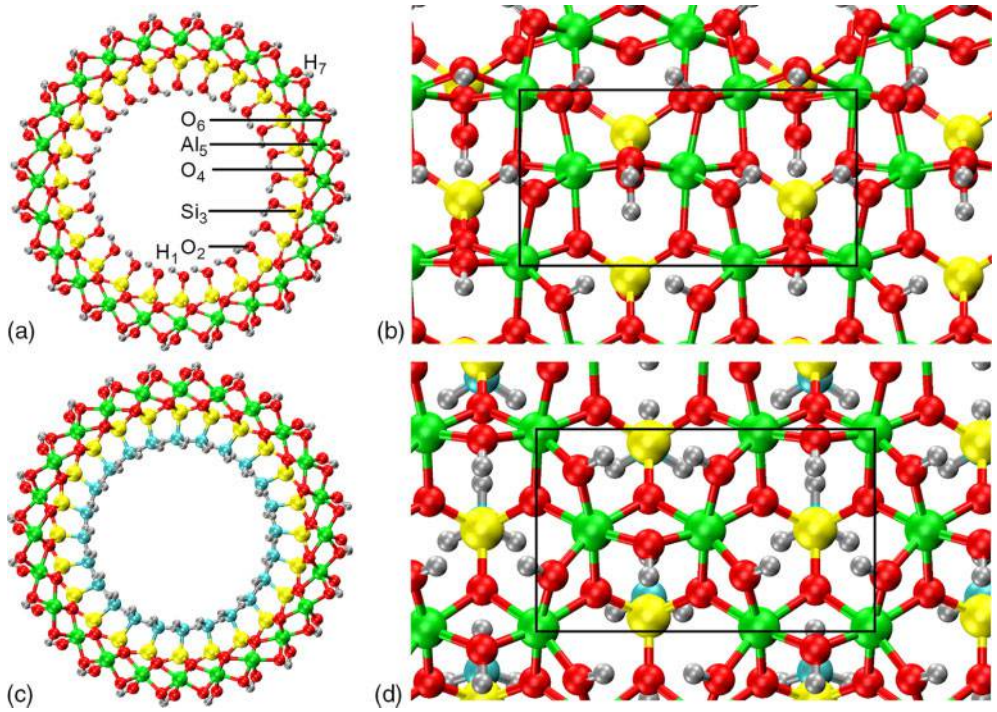


**1** ***a*** **Front view of the AlSi NT (*N*=24) structure with the adopted, layer-resolved, radial atomic labelling; *b* the AlSi wall structural motif together with the zigzag periodic unit (black line) along the nanotube axis as seen from outside the NT cavity; *c* front view of the AlSiMe NT (*N*=24) with substitution of the inner hydroxyls (—OH) by methyl groups ($-CH_3$); the AlSiMe NT wall structure is displayed in *d*. Al: green; Si: yellow; O: red; H: silver; C: cyan**

Although density functional theory (DFT) modelling and derived tight-binding approximations (TB-DFT) have assisted research in the growth mechanisms of AlSi NTs,[29,30] been used to elucidate the properties of periodic defect-free AlSi and AlGe NTs models[48–53] and to investigate possible phosphorous- and arsenic-based functionalisation,[54] the recent experimental progress in the field of Imogolite-like open-ended nanotubes (Imo-NTs) has yet to be matched by the material modelling community. With the exception of three DFT contributions focused on point defects and Fe-doping in AlSi and AlGe NTs,[50,51,55] the structural and electronic characterisation of defects, dopant and termination effects in Imo-NTs and their role in tuning the NT electronic and spectroscopic properties as well as its chemical reactivity is to date unexplored. In addition, AlSi NTs walls are experimentally known to develop an intrinsic polarisation,[56] with accumulation of negative (positive) charges on the interior (exterior) of the NT cavity (Fig. 2). Recent DFT simulations have shown this polarisation to be linked with a separation in real space of the edges of the NT valence band (VB) and conduction band (CB)[51,52] and to be independent of the substitution of Si—OH by Ge—OH in the tube interior.[51] The extent to which these peculiar AlSi and AlGe NTs properties are affected by functionalisation of the tube walls,[39–44] the encapsulation of NTs of different radii in DW AlGe NTs,[36–38] cation-vacancy induced defects[57] or by the ionic strength of the solvent is currently unknown, which motivates our interest in this class of materials.

Density functional theory-based research in the field of Imo-NTs has so far been hindered by the severe accuracy-viability compromises, which need to be faced when modelling this class of systems on academically available hardware. With a periodic unit cell containing over 300 atoms for the smallest system of the Imo-NT family, the AlSi (*N*=24) NT: 336 atoms,[34] the computational efforts required for standard plane-wave or atomic basis set simulation of these systems are, at the very least, challenging. As a result, DFT investigations of Imo-NTs have been limited to periodically repeated models of no more than one periodic ring[48–55] or fractions of the Imo-NTs.[29,30] Although reduction of the computational cost of the simulations can be obtained by using minimal (fixed)

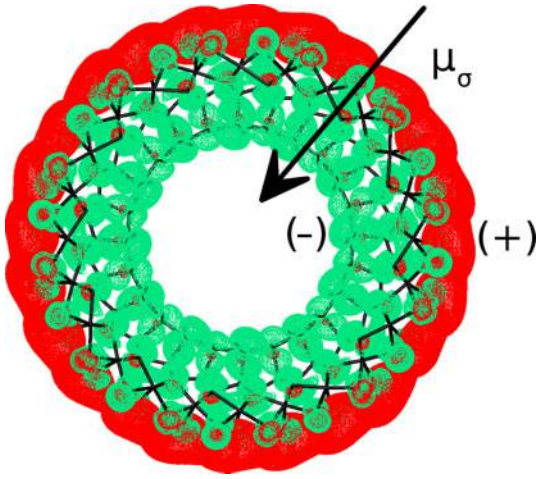


**2 Front view of the real-space separation between high-energy VB-edge (green) and low-energy CB-edge (red) in AlSi NTs. The black arrow marks the direction of the permanent surface dipole density ($\mu_\sigma$) of the NT wall with negative (positive) charge accumulation on the inner (outer) surface**

atomic basis set,[48,50,52,55] exploiting the system symmetry,[53] or resting on the transferability of TB-DFT parameterisations for analogous systems,[49,54] best practice for accurate simulation of these systems in the presence of defects, dopants, termination effects, electronic excitations and solvation by media of non-negligible ionic strength is far from being established.

The well known limitations of standard local and semi-local exchange-correlation functionals in accurate simulation of band gaps, electronic localisation and polaronic distortions in metal-oxide materials[58–60] further increase the range of challenges and accuracy-viability compromises to be faced for realistic modelling of Imo-NTs at standard DFT level. Such compromises can, however, be ameliorated by realisation of the remarkable progress made in implementations of linear-scaling DFT (LS-DFT), which have made it possible to simulate systems up to several thousand atoms at DFT level on academically available hardware.[61]

Extensive work in the development of LS-DFT implementations has produced several codes capable of LS-DFT simulation, such as ONETEP,[62–65] CONQUEST,[66,67] SIESTA,[68] OPENMX[69] and highly efficient modelling of large-scale systems as possible with BIGDFT,[70] FHI-AIMS[71] and CP2K.[72] In spite of their proved maturity and applicability, these advances have not yet benefited research in Imo-NTs and other inorganic nanotubes. With the aim of introducing LS-DFT in the field of Imo-NTs, here the authors illustrate the applicability of LS-DFT as implemented in the ONETEP programme[62–65] to this class of materials, detailing the existing accuracy-viability compromises and introducing practices to maximise the efficiency of the simulations without affecting their accuracy. The authors believe these results should be useful for future LS-DFT investigation of Imo-NTs and other nanostructured AlSi (germanate) functional materials, such as zeolites or inorganic glasses.

The manuscript is organised as follows: after a brief introduction to the ONETEP theoretical framework and to the computational procedures to optimise occupied VB and unoccupied CB states, the authors present and discuss results on the convergence of the Imo-NTs simulation with respect to key computational parameters such as the kinetic energy cutoff, the localisation radius of the basis set and the convergence threshold for geometry optimisation. The authors then examine the procedure for optimisation of the Imo-NTs CB towards computation of converged band gaps. Finally, they establish the size of the smallest possible model capable of capturing relaxation of the Imo-NTs ends in the presence of a core bulk-like region.

# Methods

## Linear-scaling DFT in ONETEP

In this section, the authors briefly present the theoretical framework behind LS-DFT and its implementation in the ONETEP programme.[62–65] The interested reader is referred to Ref. 61 for a recent review of LS-DFT methods.

Linear-scaling methods exploit the 'nearsightedness'[73,74] inherent in quantum many-body systems by exploiting the localisation of Wannier functions[75–78] or the single-particle density matrix.[77,79] ONETEP is based on the latter approach and on a formulation of DFT theory with norm-conserving pseudopotentials.[80] Within ONETEP the single-particle density matrix, $\rho(\mathbf{r}, \mathbf{r}')$, is expressed in a separable form[81,82] via atom-centred functions (Non-orthogonal Generalised Wannier functions, NWGFs[83]), $\Phi_\alpha(\mathbf{r})$, as:

$$\rho(\mathbf{r}, \mathbf{r}') = \sum\nolimits_{\alpha\beta} \Phi_\alpha(\mathbf{r})\, \mathrm{K}^{\alpha\beta}\, \Phi^*_\beta(\mathbf{r}') \quad (1)$$

$\mathrm{K}^{\alpha\beta}$ is the matrix element of the density kernel, which is non-zero only if $|r_\alpha - r_\beta| < r_c$, where $r_\alpha$ and $r_\beta$ indicate the coordinates of the centres of the Non-orthogonal Generalised Wannier functions, NWGFs $\Phi_\alpha$ and $\Phi_\beta$, and $r_c$ is a real-space cutoff length. The truncation of the density Kernel ($K^{\alpha\beta}$), leading to a sparse density matrix [$\rho(\mathbf{r}, \mathbf{r}')$] is justified by the known exponential decay of $\rho(\mathbf{r}, \mathbf{r}')$ with respect to $|\mathbf{r}-\mathbf{r}'|$ for systems with an electronic band gap,[77–79] which makes any insulating or semiconducting systems (as the Imo-NTs considered here) amenable to LS-DFT simulation.

The NGWFs are centred on the nuclear coordinates and strictly localised within a sphere of radius $R_\alpha$. Being non-orthogonal, the NGWFs are characterised by a non-diagonal overlap matrix, $S_{\alpha\beta}$:

$$S_{\alpha\beta} = \int \mathrm{d}\mathbf{r}\, \Phi^*_\alpha(\mathbf{r})\, \Phi_\beta(\mathbf{r}) \quad (2)$$

The NGWFs are in turn expanded as a linear combination, of coefficients $C_{m\alpha}$, of localised yet orthogonal periodic cardinal sine (psinc) functions,[83] $D_m(\mathbf{r})$, as:

$$\Phi_\alpha(\mathbf{r}) = \sum\nolimits_m C_{m\alpha}\, \mathrm{D}_m(\mathbf{r} - \mathbf{r_m}) \quad (3)$$

with $m$ indexing the real-space Cartesian grid inside the spherical localization region of $\Phi_\alpha$. The psinc functions are formed from discrete sum of plane waves, which makes the set of $D_m(\mathbf{r})$ independent from the nuclear coordinates and systematically improvable on increase of the kinetic energy cutoff.[83] In the ONETEP approach, the total DFT energy is minimised self-consistently with respect to $K^{\alpha\beta}$ and $C_{m\alpha}$ in two nested loops.[62–65] As a result, the NGWFs are optimised *in situ* by iteratively improving the set of coefficients $C_{m\alpha}$ that minimise the total energy under the constraints of idempotency of the density matrix (equation (1)) and conservation of the number of electrons in the simulated system. The approach has been shown to lead to near complete convergence of the DFT optimisation with respect to the basis set even for minimal number of NGWFs employed in the simulations.[84]

An alternative approach to self-consistent energy minimisation is to instead employ a single loop that optimises the elements of $K^{\alpha\beta}$ only, maintaining the NGWFs fixed. Recent additions to ONETEP allows generation of suitable multiple-zeta basis sets out of pseudoatomic orbitals (PAOs), which can also be used with high accuracy given a large enough basis and the explicit calculation of the Pulay forces arising from incomplete optimisation of the basis set.[85]

As discussed in Refs. 62–65, the convergence of the ONETEP approach can depend on interlinked computational factors such as the kinetic energy cutoff, the number of NGWFs ($\Phi_\alpha$)/atom and their localisation radius, which makes a preliminary study of the convergence of the procedure for each new system necessary for efficient use of ONETEP.

### Optimisation of empty Kohn–Sham (KS) states in ONETEP

The nested loops optimisation of the DFT energy, density matrix [$\rho(\mathbf{r}, \mathbf{r}')$], density kernel ($K^{\alpha\beta}$) and NGWFs ($\Phi_\alpha$) allows linear-scaling solution of the KS DFT problem for systems with a non-zero electronic band gap without explicit reference to individual KS states as typical for standard plane-wave DFT. Kohn–Sham states can, however, be recovered from a single diagonalisation of the Hamiltonian at the end of a converged calculation.[86] Although capable of accurate computation of occupied KS states, the approach nevertheless results in poor description of unoccupied KS states since the NWGFs are optimised to describe only the occupied KS states, thence $\rho(\mathbf{r}, \mathbf{r}')$. As a result, the description of empty KS states in terms of both energy and real-space amplitude, obtained from the standard optimisation of valence NGWFs, can be extremely poor, especially for higher energy empty KS states.[86]

To overcome this limitation, which prevents sound calculation of KS DFT band gaps, and extension towards time-dependent (TD-DDFT) or perturbative post-DFT GW approaches,[87] ONETEP implements a procedure for the optimisation of a second set of atom-centred conduction-NGWFs ($\chi_\alpha$) to correctly compute empty KS from pre-optimised valence NGWFS ($\Phi_\alpha$) and ensuing density matrix [$\rho(\mathbf{r}, \mathbf{r}')$]. The approach, described in Ref. 86, is based on the optimisation of a selected number of empty KS states via nested minimisation of the energy of a conduction-projected Hamiltonian $\left(H_\chi^{\mathrm{p}}\right)$ and is given by:

$$E = \mathrm{Tr}\left[M\, H_\chi^{\mathrm{p}}\right] \tag{4}$$

with respect to the conduction-NGWFs ($\chi_\alpha$) and related density kernel ($M^{\alpha\beta}$). $H_\chi^{\mathrm{p}}$ is obtained from valence NGWFs ($\Phi_\alpha$), density kernel $K^{\alpha\beta}$ and overlap matrix ($S_\Phi$, equation (2)):

$$\begin{aligned} H_\chi^{\mathrm{p}} =& (H_\chi)_{\alpha\beta} - (T^\dagger K H_\Phi K T)_{\alpha\beta} \\ &+ \sigma (T^\dagger K S_\Phi K T)_{\alpha\beta} \end{aligned} \tag{5}$$

$H_\chi$ is the unprojected conduction Hamiltonian, $T_{\alpha\beta} = \int \mathrm{d}r\, \Phi_\alpha^*(\mathbf{r})\, \chi_\beta(\mathbf{r})$ is the cross-overlap between valence- and conduction-NGWFs, and $\sigma$ is an energy shift applied to ensure the applicability of the procedure also to initially positive eigenvalues of the (unprojected) conduction Hamiltonian. In analogy with the optimisation of the valence density Kernel ($K^{\alpha\beta}$), and especially for low-energy empty KS with some degree of localisation, $M^{\alpha\beta}$ can be meaningfully truncated on the basis of some real-space cutoff, allowing the procedure to scale linearly with the size of the modelled system.

Once the conduction-NGWFs have been optimised, the KS–Hamiltonian can be computed and diagonalised in a joint basis encompassing both valence- ($\Phi_\alpha$) and conduction- ($\chi_\alpha$) optimised NGWFs, yielding eigenvalues in very good agreement with the results from standard plane-wave DFT (for the occupied and optimised empty KS state). Besides, the definition of KS band gaps, the optimised conduction-KS states can additionally be used for calculation of optical spectra via Fermi's golden rule[87] or within the linear-response time-dependent DFT framework recently implemented in ONETEP.[88]

As explained in Ref. 87, also the convergence of this procedure can be affected by several factors such as the energy and number of the optimised conduction-KS states, the similarity between valence and conduction-KS states, the number of conduction-NGWFs ($\chi_\alpha$)/atom and their localisation radius, which makes a preliminary study of the convergence of the procedure for each new system necessary for efficient use of ONETEP.

### Further computational details

All the simulations were performed with the Perdew, Burke, Ernzerhhof (PBE) functional[89] and separable (Kleiman–Bylander) norm-conserving pseudopotentials,[90] constructed with the opium code.[91] Unless specified otherwise, the adopted kinetic energy cutoff was 1000 eV and 4 (9) valence or conduction-NGWFs were used for O (Al, Si) atoms. One NGWF was used for H atoms. In all cases, no truncation of the density kernel ($K^{\alpha\beta}$) was enforced. Based on the reported convergence tests (below), the localisation radius for all the NGWFs was 8 Bohr, unless stated otherwise. All simulations were performed with periodic boundary conditions ensuring at least 15 Å vacuum separation between replicated images along the non-periodic directions.

Geometry relaxations were executed via the quasi-Newton optimisation scheme based on the Broyden–Fletcher–Goldfarb–Shanno (BFGS) algorithm.[92] In all cases, Pulay corrections because of residual optimisation of the valence NGWFs[85] were included in the geometry optimisation.

All the simulations made use of the hybrid MPI-OpenMP parallelism recently implemented in the ONETEP programme.[93]

## Results and Discussion

### Convergence with respect to kinetic energy cutoff and NGWFs localisation radius

As explained in the Methods section, the numerical precision of the ONETEP approach in solving the KS problem depends on the number and localisation radius ($R_\alpha$) of the NGWFs used to represent $\rho(\mathbf{r}, \mathbf{r}')$ (equation (1)), as well as the kinetic energy cutoff, which is used to set up the real-space grid for the psinc expansion of the NGWFs (equation (3)).[83,84,86] To fine tune the balance between simulation accuracy and costs, it is thus necessary to study the convergence of the DFT energy with respect to these computational parameters. This is especially important when modelling a material with ONETEP for the first time, as in the case of the Imo-NTs considered here.

Our tests were performed on the basis of two models. The first one was a reduced one-dimensional (1D)-periodic model system of $Al_{12}Si_6O_{52}H_{44}$ stoichiometry, extracted from the plane-wave DFT optimised AlSi structure in Ref. 50 and kept fixed to preserve the pristine curvature of the NT structure (Fig. 3). Peripheral hydroxyls were replaced by $H_2O$ molecules to maintain the overall electroneutrality of the system. The second model was the periodic AlSiMe ($N$=24) NT displayed in Fig. 1.

Starting with the NT fragment, use of a 1000 eV kinetic energy cutoff and of 8 Bohr ($a_0$) localisation radius ($R_\alpha$) for the NGWFs yields a final DFT energy converged to within 1 meV/atom with respect to the results for a 1400 eV cutoff (Table 1). Although tighter levels of convergence are achievable, they are obtained

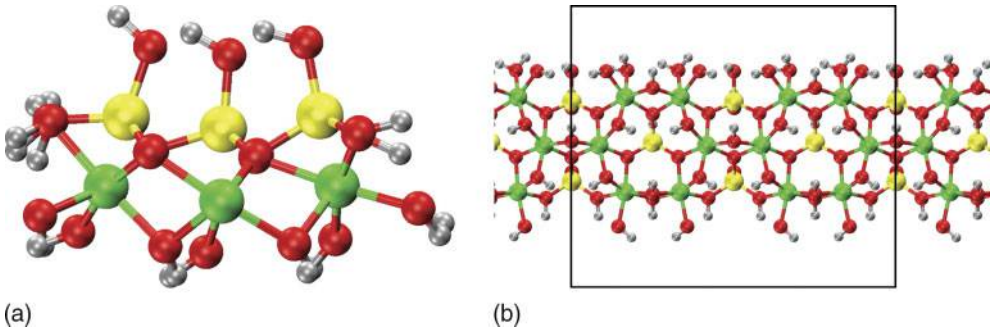


**3 Front *a* and top *b* view of the 1D-periodic $Al_{12}Si_6O_{52}H_{44}$ AlSi-NT warped fragment used for the NGWFs-convergence tests. The black rectangle in *b* indicates the periodic unit cell. Same atom-colour labelling as in Fig. 1**

at the cost of increased computation time so that on balance 1000 eV cutoff emerges as a reasonable compromise.

A similar convergence rate is found for the DFT energy for $R_\alpha$ in the 8–10$a_0$ range. Owing to the use of 4 (9) NGWFs on each of O (Al, Si) atom in the system, increase of $R_\alpha$ impacts on the simulation time more heavily than the kinetic energy cutoff because of the larger number of psinc grid-points included in the NGWF localisation region (equation (3)), and the ensuing increase in the number of steps required to optimise the coefficients of the NGWFs. Based on these results, use of 8 Bohr NGWFs localisation radius ($R_\alpha$) and a kinetic energy cutoff of 1000 eV appears to provide the optimal tradeoff between precision of the DFT solution and computation time. On a more specialist note, timings were measured for simulations run with 12 MPI processes and two OpenMP threads/MPI process on two 2·7 GHz, 12-core E5-2697-v2 (Ivy Bridge) series processors (no hyper-threading), and different performances may be obtained by further, hardware-dependent, fine-tuning of the MPI-OpenMP parallelism[93] on other HPC systems.

The authors also considered the dependence of the computed DFT energy on the kinetic energy cutoff for a whole-NT model. Figure 4 shows the convergence of the DFT energy with respect to the kinetic energy cutoff for the AlSiMe NT with 24 Al-atoms in the tube circumference (Fig. 1) and $R_\alpha$=8 $a_0$. In addition in this case, comparison between the results for 1000, 1300 and 1500 eV cutoff indicates an acceptable level of convergence (~2 meV/atom) for 1000 eV. Noticeably tighter convergence (<0·5 meV/atom) can be attained for moderate

**Table 1 Convergence of the density functional theory (DFT) energy for the 1D-periodic $Al_{12}Si_6O_{52}H_{44}$ fragment as a function of the kinetic energy cutoff (eV) and the NGWFs-localisation radius ($R_{\alpha,\ a0}$)**

| Cutoff (eV), $R_\alpha$ ($a_0$) | $\Delta E$ (meV/atom) | $N_{it}$ | $\Delta t$ |
|---|---|---|---|
| 800, 8 | 26·16 | 19 | −50% |
| 1000, 8 | 1·09 | 18 | −26% |
| 1200, 8 | 0·72 | 17 | −17% |
| 1400, 8 | 0 | 15 | 0 |
| 1000, 8 | 0·91 | 19 | −69% |
| 1000, 9 | 0·03 | 20 | −58% |
| 1000, 10 | 0 | 32 | 0 |

$\Delta E$: the relative energy (meV/atom) with respect the adopted energy reference ($\Delta E$=0); $N_{it}$: number of NGWFs optimisation required to converge the DFT solution to $<10^{-4}$ eV/atom; $\Delta t$: percentage computational speed-up with respect to the adopted reference.

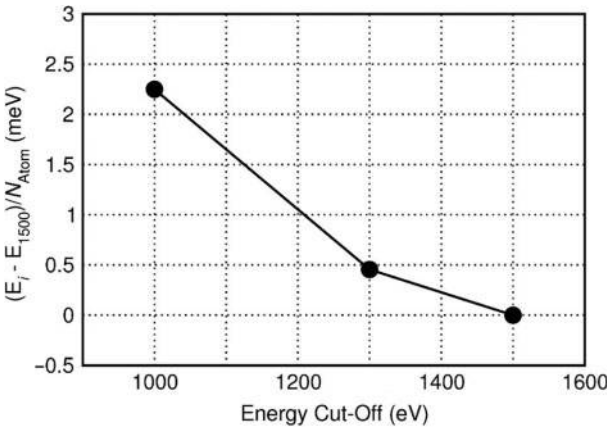


**4 Convergence of the AlSiMe NT ($N$=24) DFT energy with respect to the adopted kinetic energy cutoff**

increase of the kinetic energy cutoff over 1200 eV, which however leads to increase of the computation time. On the basis of these results, we adopted a kinetic energy cutoff of 1000 eV and $R_\alpha$=8$a_0$ for the following benchmarks.

## Optimisation of the NT periodic unit

The authors now illustrate the procedure for optimisation of the NT repeat unit length with ONETEP, focusing on the AlSiMe NT ($N$=24) displayed in Fig. 1. Based on earlier plane-wave DFT reports regarding weak dependence of this parameter on the reciprocal-space sampling in the simulations, with optimal convergence obtained for 2$k$ points along the NT periodic direction,[47] in our tests we adopted an equivalent set-up based on a x2 supercell of the AlSiMe NT along the tube axis. The localisation radius of the NGWFs was set to 8$a_0$, on the basis of the good convergence of the DFT energy tested in Table 1.

In order to maintain the translational invariance of the system with respect to the discretised psinc grid (avoiding the emergence of the 'egg-box' effect[95,96]), and following, Ref. 97, the unit cell length along the tube axis ($c$, Fig. 1) was expanded and contracted in multiple of the psinc spacing. In each case, all the atomic positions were optimised to within a 0·05 eV/Å convergence threshold.

The energy for the optimised geometries is plotted in Fig. 5 as a function of $c$. Quadratic fitting of the calculated values suggests an energy minimum for $c$=8·64±0·01 Å, which is very close to the optimised $c$-value for the $N$=24 AlSi NT (8·68±0·01 Å),[51] suggesting a predominant role of the aluminium-hydroxide backbone, rather than the inter-silanol hydrogen bonding network or methyl pending

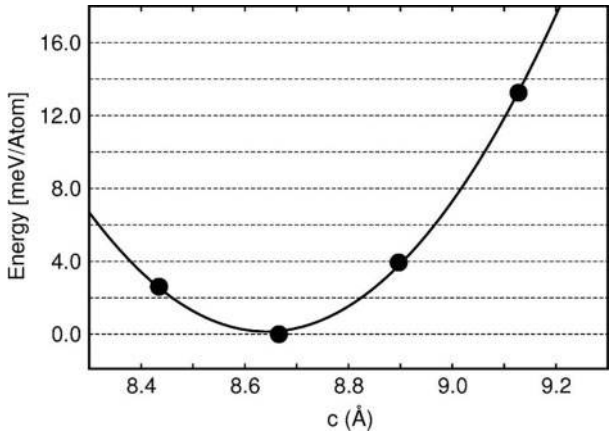


**5 Energy of the optimised AlSiMe NT ($N$=24) as a function of the tube repeat unit length $c$. The continuous line shows the results of a quadratic fitting to the density functional theory (DFT) energies (points)**

groups, in controlling the optimised length of the tube, at least at PBE level. Inline with experimental results,[43] optimisation of the $c$-parameter and atomic position for AlSiMe NTs of *different* diameter ($N$) reveals the occurrence of a shallow energy minimum for diameters larger ($28 < N < 32$, depending on the adopted functional and ensuing treatment of dispersion interactions) than for the AlSi NT ($N$=24). These results will be reported elsewhere.[98]

Finally, on a more technical note, the authors report that in out tests the energy of the 0·1 eV/Å optimised systems were found to be converged within $<10^{-5}$ eV/atom with respect to the results of the 0·05 eV/Å optimisation, suggesting an 0·1 eV/Å optimisation threshold as viable for Imo-NTs.

## Optimisation of the NT CB and band gap

As described in the Methods section, optimisation of empty KS states in ONETEP is achieved via dedicated post-processing of the optimised (valence) density matrix and KS energy. The user has control over the number of empty KS states to be optimised as well as the number and localisation radius of the conduction-NGWFs ($\chi_\alpha$) used to represent them, with fewer states and (more compact) NGWFs requiring less computational resources at the potential cost of accuracy.[87] Here, the authors present results on the convergence of the AlSiMe ($N$=24, Fig. 1) band gap with respect to the number of empty KS optimised for an x1 supercell at the minimum energy $c$-value (Fig. 5).

The authors tested the convergence of the band gap computed on the joint $\Phi_\alpha$ and $\chi_\alpha$ representation (see Methods section) following optimisation of 10, 20, 30 and 40 empty KS states. The results are displayed in Fig. 6. The low-energy edge of the CB obtained with 30 optimised KS is found to deviate by $<9$ meV with respect to the results for 40 optimised empty KS states. Optimisation of 20 (10) empty KS leads to a poorer convergence of 18 eV (32 meV) for the computed CB edge. The converged band gap for the AlSiMe NT, calculated as energy difference between the low-energy CB edge and high-energy VB edge with 40 optimised conduction-KS states is 4·75 eV, 0·18 eV wider than for the pristine AlSi NTs ($N$=24) at the same level of theory. Thus, the methylation of AlSi NTs leads to an increase of the NT band gap with respect to the hydroxylated case. Electrostatic alignment between AlSi and AlSiMe NTs reveals a negative shift of −0·34 eV (−0·16 eV) for the AlSiMe NT VB (CB) with respect to the AlSi results, suggesting methylation of Imo-NTs as an effective strategy towards engineering of band gaps and band alignments for these materials.[97]

## Structural relaxation of the NT termination and its dependence on the size of the model

With the exception of the (non-atomically resolved) transmission electron microscopy images for AlSi and AlGe NT thin-films reported in Ref. 26, very little is currently known on the structure of the tube open-ended extremities. As a result, the available insight into termination-induced effects on the NTs' electronic properties and chemical reactivity or into the possible segregation of point defects[57] at the tube extremities is effectively non-existent.

Although the atomic structure and electronic properties of Imo-NT extremities could, in principle, be elucidated via DFT modelling, the size of the models to realistically capture the tube extremities *in vacuo* or, even more challenging, in solvent phase, has so far prevented any advance along these lines. However, as the authors demonstrate below, DFT modelling of the tube terminations can be viably and accurately performed by exploiting the ONETEP approach. For this illustrative application they consider the AlSi ($N$=24) NT.

Owing to the composition of the structural unit, $(Al_2SiO_7H_4)_N$ (Fig. 1), two neutral terminations are possible for the AlSi NTs (Fig. 7). In one case, referred to as the $AlOH_2$ termination from here onwards, the aluminium-hydroxide network of the NT is truncated and the terminal under-coordinated Al-atoms saturated with one $H_2O$ molecule (instead of one hydroxyl, —OH) to maintain electroneutrality. In the other, referred to as the SiOH termination, the NT ends with two hydroxyls connected to the fourfold coordinated terminal Si-atom, resulting in a $Si—(OH)_2$ termination. In addition, in this case, the second hydroxyl is needed to maintain electroneutrality.

In order to simulate NT ends, a suitable model should be clearly finite (i.e. not 1D-periodic as used so far for Imo-NTs[48–55]) and large enough to allow accurate description of both the *core* and *terminal* regions of the NT model. Although real Imo-NTs are 20–100-nm long depending on their composition,[26] it is reasonable to expect the relaxation of the tube terminations to involve no more than a few nanometres from the tube end. Accordingly, rather than attempting simulation of >20nm models, it is desirable to define the smallest possible system capable of simultaneous description of both the *core* and *terminal* regions of the NTs. To this end, several models were set up on the basis of the periodically optimised NT structure. As shown in Fig. 8, for both the $AlOH_2$ and SiOH terminations, we considered models of increasing size measured by the number of complete Al-hexagons (Fig. 8) present along the structure axis, which we accordingly labelled *hex-3,5* and *7*. Their overall stoichiometry and number of atoms is reported in Table 2. To prevent the occurrence of large longitudinal polarisations[99] which may affect the geometry optimisation of the systems, all the finite NTs model were symmetric with respect to a plane containing the innermost Si-ring (Ring 0 in Fig. 8).

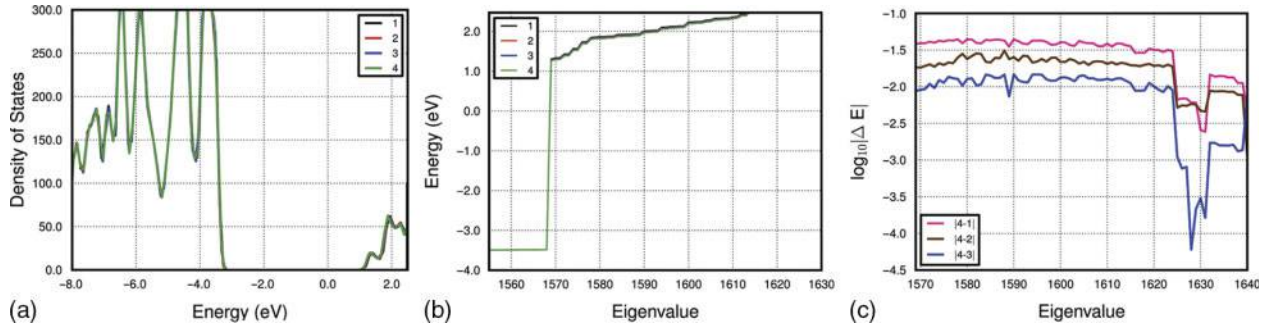


**6 Calculated density of states for the AlSiMe NT (*N*=24, Fig. 1) following optimisation of different numbers of conduction-KS *a*. 1–4 labels indicate the results for 10 (1), 20 (2), 30 (3), 40 (4) optimised conduction-KS. The energy of each KS eigenvalue is reported in *b*. Panel *c* displays, on a logarithmic scale, the eigenvalue energy differences between data sets 1–3 and 4**

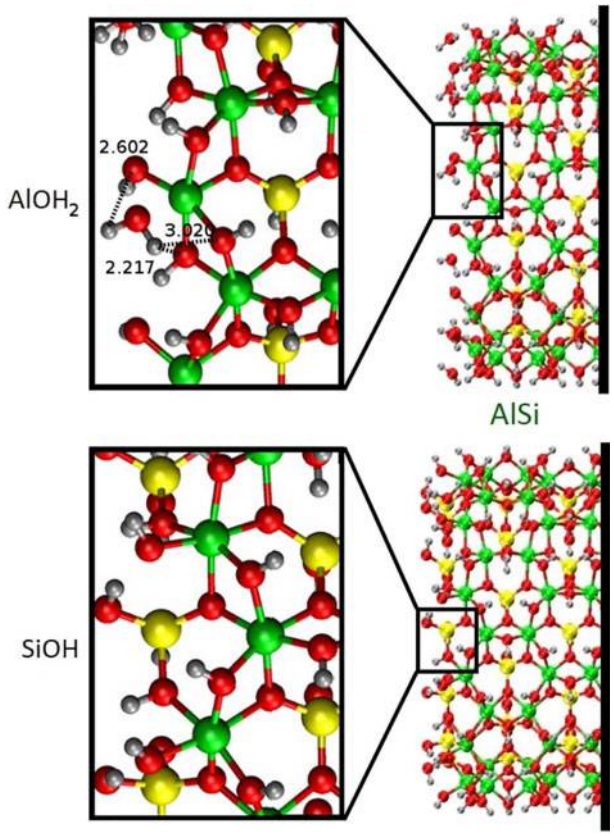


**7 Side-view of the two optimised electroneutral truncations of the AlSi NT: $AlOH_2$ termination (top) and SiOH termination (bottom). The insets display a close-up of the coordination of the terminal Al (top) and Si (bottom) atoms. For the $AlOH_2$ termination, the shortest distances (Å) between the H atoms of the coordination-$H_2O$ and the bridging hydroxyls (Al—OH—Al) have been marked as dotted lines. Same atom-colour labelling as in Fig. 1**

**Table 2 Stoichiometry of the considered models of the $AlOH_2$ and SiOH terminations of the AlSi NTs (*N*=24)**

| | $AlOH_2$ termination | SIOH termination |
|---|---|---|
| hex-3 | $Al_{96}Si_{36}O_{348}H_{264}$ (744) | $Al_{96}Si_{60}O_{396}H_{264}$ (816) |
| hex-5 | $Al_{144}Si_{60}O_{516}H_{360}$ (1080) | $Al_{144}Si_{84}O_{564}H_{360}$ (1152) |
| hex-7 | $Al_{192}Si_{84}O_{684}H_{456}$ (1416) | $Al_{192}Si_{108}O_{732}H_{456}$ (1488) |

The total number of atom is reported within brackets.

The geometry of the AlSi NT finite models was optimised relaxing all the atoms of the models, apart from the Si-atoms in the central ring ($R$=0 in Fig. 8). The latter were kept fixed at the periodically optimised geometry and used as reference for measuring the distortion of the tube along its axis.

The NT relaxation was monitored according to three geometrical descriptors. The first one is the average ring displacement, $<\Delta r(R)>$, defined as:

$$< \Delta r(R) >= N^{-1}\sum_{i}^{N}\left|\mathbf{r_i}(R) - \mathbf{r_i^b}(R)\right| \quad (6)$$

where $\mathbf{r_i}$ is the position of the $i$th atom of the $R$th ring (Fig. 8) in the finite NT model, and $\mathbf{r_i^b}$ is the position of the same atom in the periodically repeated NT model. $N$ refers to the number of atoms in a given ring. A ring is defined as the group of longitudinally equivalent Si (Al) atoms and bridging hydroxyls (OH) plus the closest hydroxyl groups facing the tube ends. For the central ring ($R$=0 in Fig. 8), only longitudinally equivalent Si-atoms and bridging OH were considered in computing $<\Delta r(0)>$. For $AlOH_2$-terminated NTs, terminal $H_2O$ molecules were not considered in the calculation of the average ring displacement. Negligible $<\Delta r>$ values correspond to negligible relaxation of the ring structure from the periodically optimised geometry and are used to identify the separation between core and terminal regions of the NT model.

The second geometrical descriptor to quantify the cross-section distortion of the NT, leading to changes in the diameter of the NT rings, is the average radial-resolved (Fig. 1) ring diameter $< D(j, R)>$, calculated as:

$$< D(j, R) >= M^{-1}\sum_{i}^{M} d_i(j, R) \quad (7)$$

where $d_i(j, R)$ indicates the layer-resolved ($j$: $H_1$, $O_2$, ..., $H_7$, see Fig. 1) diameter for the $i$th pair of atoms in the $R$th ring. Each $d_i(j, R)$ was in turn calculated as the distance between opposite atoms in the $j$th layer of the $R$th ring. $M=N/2$ is the number of layer-equivalent atom pairs in a given ring.

The third geometrical descriptor used to measure the overall longitudinal relaxation of the NT models was the tube length ($L$) along its axis (parallel to the $z$ direction) calculated as the difference in the $z$ coordinate between the terminal Al (Si) rings of the $AlOH_2$ (SiOH) terminations:

$$L = n^{-1}\sum_{i}^{n}\left[z_i(R_{max}) - z_i(R_{min})\right] \quad (8)$$

with $n$ referring to the number of atoms in the Al(Si) terminal rings (12 for the considered systems).

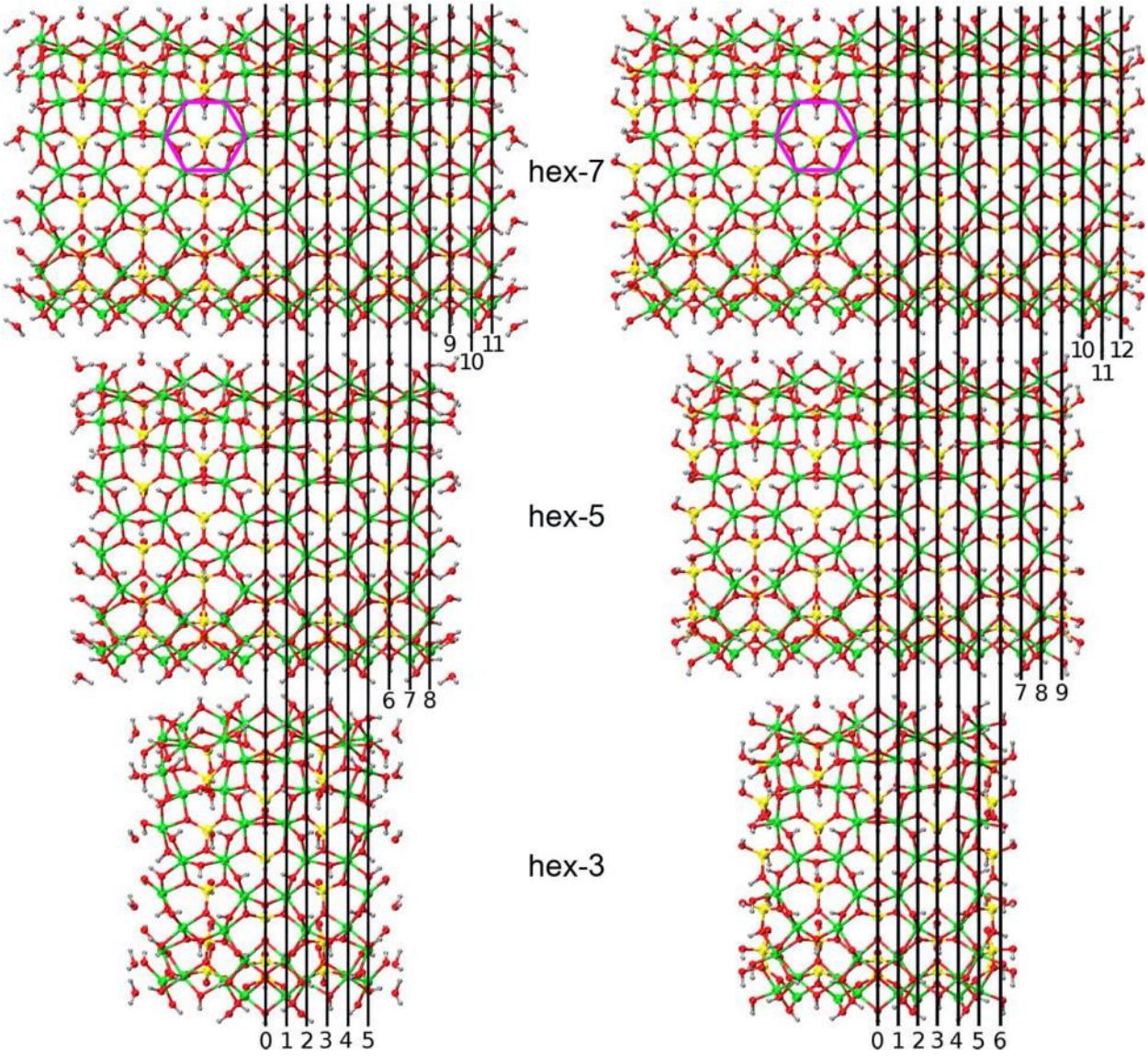


**8 The optimised atomic structure of the considered finite models for the $AlOH_2$ (left) and SiOH (right) terminations. The models are labelled (hex-3, 5, 7) according to the number of complete Al-hexagons present along the structure axis. In the top panels, one Al-hexagon has been highlighted in pink. Black vertical lines marks the position of the tube rings ($R=-12$, ..., 0, ..., 12 from left to right) with $R=0$ corresponding to the innermost Si ring. Marks for negative rings have been omitted for clarity. Same atom-colour labelling as in Fig. 1**

With an average ring displacement ($<\Delta r>$, Fig. 9) $>0{\cdot}1$ Å for the innermost rings, the hex-3 models turns out to be too small to accommodate for converged relaxation of the tube extremities in the presence of a structurally unperturbed core region. This conclusion holds regardless of the $AlOH_2$ or $Si(OH)_2$ termination. Conversely, the negligible average ring displacement ($\leqslant 10^{-3}$ Å) for at least the 3 (5) innermost rings of the hex-5 (hex-7) models demonstrates that these larger models are indeed suitable for describing relaxation of the tube ends in the presence of a bulk-like core. It is interesting to note that, both for the hex-5 and hex-7 models, the $AlOH_2$ termination is calculated to induce larger structural relaxation than the $Si(OH)_2$ termination, because of the larger disruption to the aluminium-hydroxide network and NT-VB.[50]

Radial- and ring-resolved analysis of the relaxed diameters ($<D(j, R)>$, Fig. 10) reveals an overall tendency for the NT ends to relax inwards, making the cavity narrower at the NT extremities. The simulations for the larger hex-5 (7) models suggest the tube-end relaxation mechanism to be affected by the specific ($AlOH_2$ or SiOH) termination, leading to different changes for radially different atoms. Whereas relaxation of the (hex-7) $AlOH_2$ termination proceeds via major contraction of the $O_2$, $Si_3$ and $O_4$ diameters, geometry optimisation of the SiOH termination is found to affect mainly the $Al_5$ and $O_6$ layers.

Inline with the calculated $<\Delta r>$, also the calculated $<D(j, R)>$ points out severe biases in the optimisation of the smallest hex-3 models. With deviations up to $>2$ Å ($O_4$ layer) from the hex-5 (7) optimised terminal diameters, the hex-3 model turns out to be clearly too small to accurately capture the cavity narrowing at the tube extremities. These results strengthen the conclusion that, if interested in modelling termination effects in AlSi NTs in the presence of a core bulk-like region of the tube, the smallest viable model should be at least as long as the hex-5. Work is currently under way to assess whether the same conclusion holds also for other

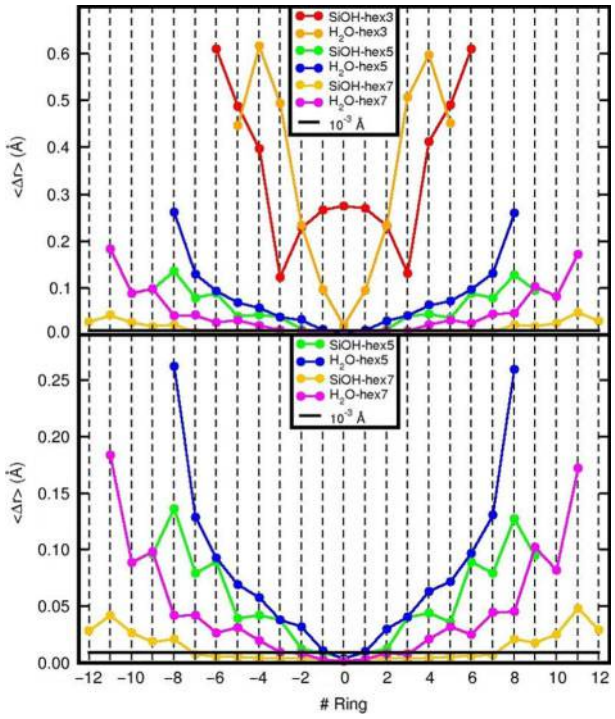


**9 Ring-resolved average displacement (<Δ*r*>,Å) for the finite (hex-3,5,7) models of the $AlOH_2$ and SiOH NT-terminations (top). The bottom panel reports a close-up of the data for hex-5 and hex-7 terminations. The black horizontal line marks the $10^{-3}$ Å displacement threshold. Same ring labelling as in Fig. 8**

members of the Imo-NTs family such as AlSiMe or AlGeMe.[100]

Turning to the variation in the NT length ($L$) following relaxation of its extremities, Table 3 shows the difference in the tube length between the optimised finite models and the periodically repeated counterparts ($\Delta L$). With $\Delta L$ values <0·05 Å, we find the relaxation of the tube terminations to negligibly affect the length (equation (8)) of hex-5 and hex-7 models, regardless of the $AlOH_2$ or SiOH termination. These results are in qualitative agreement with the regular appearance imaged for the termination of AlSi thin-films by TEM in Ref. 25, although the resolution of the experimental images does not allow quantitative comparison between experiment and simulations.

In contrast to the hex-5 and hex-7 cases, the simulations suggest the specific termination of the hex-3 models to more strongly affect the relaxed NT length. Whereas the calculated ΔL for the $AlOH_2$-terminated hex-3 model is negligibly small ($\Delta L$=0·01 Å), the axial distortion for the SiOH termination is substantially larger ($\Delta L$=1·16 Å) as a consequence of the displacement induced on the terminal Si-atoms by reorganisation of the silanol H-bonding network at the tube extremities (Fig. 11).

Overall, these results indicate that hex-5 models are sufficiently extended to suitably account for the termination-induced relaxations in AlSi NT in the presence of a bulk-like region at the core of the model. They also demonstrate that smaller models, such as the hex-3, can severely bias the simulation. Further work, currently in progress, will explore the effects of terminal relaxations on the AlSi NTs electronic structure and wall-polarisation and similarities and analogies between end-relaxations in AlSi, AlGe and AlSiMe NTs. These results will be reported elsewhere.[100]

## Summary

The authors have illustrated the applicability of the linear scaling, *in situ* optimised basis set, ONETEP approach to the emerging class of inorganic open-ended AlSi-based Imo-NTs. Study of accuracy-viability tradeoffs for representative systems of the Imo-NTs family suggests the use of 1000 eV kinetic energy cutoff and 8 Bohr localisation spheres for the optimised basis set to provide optimal accuracy-viability compromises for geometrical relaxation of these systems. The authors find optimisation of at least 30 empty KS states to be needed for convergence of the calculated band gap to <10 meV. Analysis of the optimised structure for different-sized models of the tube

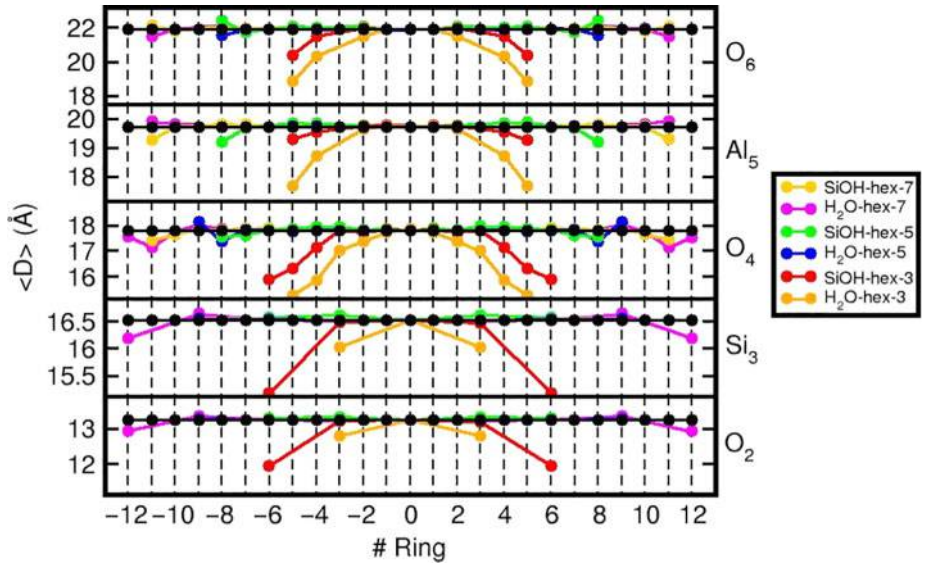


**10 The layer-resolved ($O_{2,4,6}$, $Si_3$ and $Al_5$, see Fig. 1) average ring-diameter (<*D*>,Å) for the finite (hex-3,5,7) models of the $AlOH_2$ and SiOH NT terminations. Results for the periodically optimised NT are displayed as black circles. Same ring labelling as in Fig. 8**

**Table 3 Optimised length (*L*,Å) of the finite (hex-3,5,7) models of the $AlOH_2$ and SiOH NT terminations**

| | $AlOH_2$ termination | SiOH termination |
|---|---|---|
| hex-3 | 14·40 (+0·01) | 16·15 (+1·16) |
| hex-5 | 23·07 (+0·01) | 26·00 (+0·00) |
| hex-7 | 31·68 (+0·05) | 34·35 (+0·02) |

The change with respect to the length of the corresponding periodic models ($\Delta L$,Å) is reported in brackets. Axial NT contraction (expansion) corresponds to positive (negative) values of $\Delta L$. Same model and termination labelling as in Fig. 8.

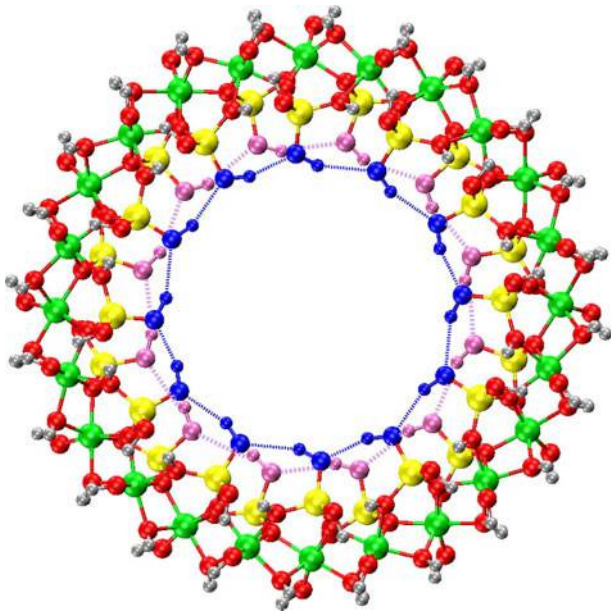

**11 Front view of the relaxed SiOH termination of the hex-3 model. The outermost (blue) and second outermost (pink) H-bonding networks between pending silanol groups have been marked by dotted lines. Same atom-colour labelling as in Figs. 1 and 8 apart from the terminal (blue) and next to terminal (pink) hydroxyl groups**

extremities reveals heavy biases in the simulation for systems $<2$ nm ($\sim$1100 atoms), making use of highly efficient DFT implementations a requirement for accurate simulation of the NT terminations. Overall, we find the NT extremities to relax inwards leading to a narrower cavity at the tube extremities, with minimal effects on the NT length. The authors believe these results should be useful for future LS-DFT investigation of other members of the Imo-NTs family as well as for simulation of other AlSi-based functional materials.

## Acknowledgements

Support from EPSRC-UK (EP/I004483/1) is gratefully acknowledged. This work made use of the N8 (EPSRC EP/K000225/1), ARCHER (via the UKCP Consortium, EP/K013610/1) and the STFC Hartree Centre (Daresbury Laboratory, UK) High Performance Computing facilities. The STFC Hartree Centre is a research collaboratory in association with IBM providing high performance computing platforms funded by the UK's investment in e-Infrastructure.

## References

1. S. Iijima: *Nature*, 1991, **354**, (6348), 56–58.
2. R. H. Baughman: *Science*, 2000, **290**, (5495), 1310–1311.
3. M. S. Dresselhaus and H. Dai: *MRS Bull.*, 2004, **29**, (4), 237–281.
4. M. Remskar: *Adv. Mater.*, 2004, **16**, (17), 1497–1504.
5. R. Tenne and C. N. R. Rao: *Phil. Trans. R. Soc. A*, 2004, **362**, (1823), 2099–2115.
6. A. Bianco, K. Kostarelos and M. Prato: *Curr. Opin. Chem. Biol.*, 2005, **9**, (6), 674–679.
7. P. Singh, S. Campidelli, S. Giordani, D. Bonifazi, A. Bianco and M. Prato: *Chem. Soc. Rev.*, 2009, **38**, (8), 2214–2230.
8. P. C. Ma, N. A. Siddiqui, G. Marom and J. K. Kim: *Compos. A*, 2010, **41**, (10), 1345–1367.
9. N. Karousis, N. Tagmatarchis and D. Tasis: *Chem. Rev.*, 2010, **110**, (9), 5366–5397.
10. H. Kuzmany, A. Kukovecz, F. Simon, M. Holzweber, C. H. Kramberger and T. Pichler: *Synth. Met.*, 2004, **141**, (1–2), 113–122.
11. D. Vairavapandian, P. Vichchulada and M. D. Lay: *Anal. Chim. Acta*, 2008, **626**, (2), 119–129.
12. S. Singh and P. Kruse: *Int. J. Nanotechnol.*, 2008, **5**, (9–12), 900–929.
13. K. Yanagi, K. Iakoubovskii, H. Matsui, H. Matsuzaki, H. Okamoto, Y. Miyata, Y. Maniwa, S. Kazaoui, N. Minami and H. Kataura: *J. Am. Chem. Soc.*, 2007, **129**, (16), 4992–4997.
14. M. Majumder, N. Chopra and B. J. Hinds: *ACS Nano.*, 2011, **5**, (5), 3867–3877.
15. T. W. Chamberlain, J. C. Meyer, J. Biskupek, J. Leschner, A. Santana, N. A. Besley, E. Bichoutskaia, U. Kaiser and A. N. Khlobystov: *Nat. Chem.*, 2011, **3**, (9), 732–737.
16. G. Giambastiani, S. Cicchi, A. Giannasi, L. Luconi, A. Rossin, F. Mercuri, C. Bianchini, A. Brandi, M. Melucci, G. Ghini, P. Stagnaro, L. Conzatti, E. Passaglia, M. Zoppi, T. Montini and P. Fornasiero: *Chem. Mater.*, 2011, **23**, (7), 1923–1938.
17. W. Lu and C. M. Lieber: *Nat. Mater.*, 2007, **6**, (11), 841–850.
18. X. Pan, Z. Fan, W. Chen, Y. Ding, H. Luo and X. Bao: *Nat. Mater.*, 2007, **6**, (7), 507–511.
19. J. Kong, N. R. Franklin, C. W. Zhou, M. G. Chapline, S. Peng, K. J. Cho and H. J. Dai: *Science*, 2000, **287**, (5453), 622–625.
20. W. A. De Heer, A. Châtelain and D. Ugarte: *Science*, 1995, **270**, (5239), 1179–1180.
21. A. Srivastava, O. N. Srivastava, S. Talapatra, D. R. Vajtai and P. M. Ajayan: *Nat. Mater.*, 2004, **3**, (9), 610–614.
22. D. W. Wang, H. T. Fang, F. Li, Z. G. Chen, Q. S. M. Zhong, G. Q. Lu and H. Cheng: *Adv. Funct. Mater.*, 2008, **18**, (23), 3787–3793.
23. J. Goldberger, R. Fab and P. D. Yang: *Acc. Chem. Res.*, 2006, **39**, (4), 239–248.
24. S. I. Wada, A. Eto and K. Wada: *J. Soil Sci.*, 1979, **30**, (2), 347–355.
25. P. F. Barron, M. A. Wilson, A. S. Campbell and R. L. Frost: *Nature*, 1982, **299**, (5884), 616–618.
26. S. Mukherjee, V. M. Bartlow and S. Nair: *Chem. Mater.*, 2005, **17**, (20), 4900–4909.
27. D. Y. Kang, J. Zang, E. R. Wright, A. L. McCanna, C. W. Jones and S. Nair: *ACS Nano.*, 2010, **4**, (8), 4897–4907.
28. B. K. G. Theng, M. Russell, G. J. Churchman and R. L. Parfitt: *Clays Clay Miner.*, 1982, **30**, (2), 143–149.
29. S. Mukherjee, K. Kim and S. Nair: *J. Am. Chem. Soc.*, 2007, **129**, (21), 6820–6826.
30. G. I. Yucelen, R. P. Choudhury, A. Vyalikh, U. Scheler, H. W. Beckham and S. Nair: *J. Am. Chem. Soc.*, 2011, **133**, (14), 5397–5412.
31. G. I. Yucelen, D. Y. Kang, R. C. Guerrero-Ferreira, E. R. Wright, H. W. Beckham and S. Nair: *Nano. Lett.*, 2012, **12**, (2), 827–832.
32. P. D. Cradwick, K. Wada, J. D. Russell, N. Yoshinaga, C. R. Masson and V. C. Farmer: *Nat. Phys. Sci.*, 1972, **240**, (104), 187–189.
33. L. A. Bursill, J. L. Peng and L. N. Bourgeois: *Phil. Mag. A*, 2000, **80**, (1), 105–117.
34. S. Konduri, S. Mukherjee and S. Nair: *Phys. Rev. B*, 2006, **74**, (3), 033401.
35. C. Levard, J. Rose, A. Thill, A. Masion, E. Doelsch, P. Maillet, O. Spalla, L. Olivi, A. Cognigni, F. Ziarelli and J. Y. Bottero: *Chem. Mater.*, 2010, **22**, (8), 2466–2473.
36. P. Maillet, C. Levard, O. Spalla, A. Masion, J. Rose and A. Thill: *Phys. Chem. Chem. Phys.*, 2011, **13**, (7), 2682–2689.
37. A. Thill, P. Maillet, B. Guiose, O. Spalla, L. Belloni, P. Chaurand, M. Auffan, L. Olivi and J. Rose: *J. Am. Chem. Soc.*, 2012, **134**, (8), 3780–3786.

38. M. -S. Amara, E. Paineau, M. Bacia-Verloop, M. -E. M. Krapf, P. Davidson, L. Belloni, C. Levard, J. Rose, P. Launois and A. Thill: *Chem. Comm.*, 2013, **49**, (96), 11284–11286.
39. D. Y. Kang, J. Zang, C. W. Jones and S. Nair: *J. Phys. Chem. C*, 2011, **115**, (15), 7676–7685.
40. C. Zanzottera, M. Armandi, S. Esposito, E. Gorrone and B. Bonelli: *J. Phys. Chem. C*, 2012, **116**, (38), 20417–20425.
41. C. Zanzottera, A. Vicente, E. Celasco, C. Fernandez, E. Garrone and B. Bonelli: *J. Phys. Chem. C*, 2012, **116**, (25), 7499–7508.
42. B. Bonelli, M. Armandi and E. Garrone: *Phys. Chem. Chem. Phys.*, 2013, **15**, (32), 13381–13390.
43. I. Bottero, B. Bonelli, S. E. Ashbrook, P. A. Wright, W. Zhou, M. Tagliabue, M. Armandi and E. Garrone: *Phys. Chem. Chem. Phys.*, 2011, **13**, (2), 744–750.
44. D. Y. Kang, N. A. Brunelli, G. I. Yucelen, A. Venkatasubramanian, J. Zang, J. Leisen, P. J. Hesketh, C. W. Jones and S. Nair: *Nat. Comm.*, 2014, **5**, 3342–3351.
45. K. Katsumata, X. Hou, M. Sakai, A. Nakajima, A. Fujishima, N. Matsushita, K. J. D. MacKenzie and K. Okada: *Appl. Catal B Environ.*, 2013, **138**, (4), 243–252.
46. L. L. Marzan and A. P. Philipse: *Colloid Surf. A*, 1994, **90**, (1), 95–109.
47. W. Ma, W. O. Yah, H. Otsuka and A. Takahara: *J. Mater. Chem.*, 2012, **22**, (24), 11887–11892.
48. F. Alvarez-Ramírez: *Phys. Rev. B.*, 2007, **76**, (12), 125421.
49. L. Guimarães, A. N. Enyashin, J. Frenzel, T. Heine, H. A. Duarte and G. Seifert: *ACS Nano*, 2007, **1**, (4), 362–368.
50. L. Li, Y. Xia, M. Zhao, C. Song, J. Li and X. Liu: *Nanotechnology*, 2008, **19**, (17), 175702–175711.
51. G. Teobaldi, N. S. Beglitis, A. J. Fisher, F. Zerbetto and W. A. Hofer: *J. Phys. Condens. Matter.*, 2009, **21**, (19), 195301–195310.
52. M. Zhao, Y. Xia and L. Mei: *J. Phys. Chem. C*, 2009, **113**, (33), 14834–14837.
53. R. Demichelis, Y. Noël, P. D'Arco, L. Maschio, R. Orlando and R. Dovesi: *J. Mater. Chem.*, 2010, **20**, (46), 10417–10425.
54. L. Guimarães, Y. N. Pinto, M. P. Lourenço and H. A. Duarte: *Phys. Chem. Chem. Phys.*, 2013, **15**, (12), 4303–4309.
55. F. Alvarez-Ramírez: *J. Chem. Theory Comput.*, 2009, **5**, (12), 3224–3231.
56. J. P. Gustafsson: *Clays Clay Miner.*, 2001, **49**, (1), 73–80.
57. G. I. Yucelen, R. P. Choudhury, J. Leisen, S. Nair and H. W. Beckham: *J. Phys. Chem. C*, 2012, **116**, (32), 17149–17157.
58. G. Pacchioni, F. Frigoli, D. Ricci and J. A. Weil: *Phys. Rev. B.*, 2000, **63**, (1), 054102.
59. A. M. Stoneham, J. Gavartin, A. L. Shluger, A. V. Kimmel1, D. Muñoz, D. Muñoz Ramo1, H. M. Rønnow, G. Aeppli and C. Renner: *J. Phys.*, 2007, **19**, (25), 255208–255230.
60. S. Lany and A. Zunger: *Phys. Rev. B.*, 2009, **80**, (8), 085202.
61. D. R. Bowler and T. Miyazaki: *Rep. Prog. Phys.*, 2012, **75**, (3), 036503–036547.
62. C. K. Skylaris, P. D. Haynes, A. A. Mostofi and M. C. Payne: *J. Chem. Phys.*, 2005, **122**, (8), 084119.
63. P. D. Haynes, C. K. Skylaris, A. A. Mostofi and M. C. Payne: *Phys. Status Solidi B*, 2006, **243**, (11), 2489–2499.
64. N. D. M. Hine, P. D. Haynes, A. A. Mostofi, K. Skylaris and M. C. Payne: *Comput. Phys. Commun.*, 2009, **180**, (7), 1041–1053.
65. N. D. M. Hine, M. Robinson, P. D. Haynes, C. K. Skylaris, M. C. Payne and A. A. Mostofi: *Phys. Rev. B.*, 2011, **83**, (19), 195102.
66. D. R. Bowler, R. Choudhury, M. J. Gillan and T. Miyazaki: *Phys. Status Solidi B*, 2006, **243**, (5), 989–1000.
67. M. J. Gillan, D. R. Bowler, A. S. Torralba and T. Miyazaki: *Comput. Phys. Commun.*, 2007, **177**, (1–2), 14–18.
68. J. M. Soler, E. Artacho, J. D. Gale, A. Garcia, J. Junquera, P. Ordejon and D. Sanchez-Portal: *J. Phys.*, 2002, **14**, (11), 2745–2779.
69. T. Ozaki and H. Kino: *Phys. Rev. B*, 2005, **72**, (4), 045121.
70. S. Mohr, L. E. Ratcliff, P. Boulanger, L. Genovese, D. Caliste, T. Deutsch and S. Goedecker: *J. Chem. Phys.*, 2014, **140**, (20), 204110.
71. V. Blum, R. Gehrke, F. Hanke, P. Havu, V. Havu, X. Ren, K. Reuter and M. Scheffler: *Comput. Phys. Commun.*, 2009, **180**, (11), 2175–2196.
72. J. Hutter, M. Iannuzzi, F. Schiffmann and J. VandeVondele: *WIREs Comput. Mol. Sci.*, 2014, **4**, (1), 15–25.
73. W. Kohn: *Phys. Rev. Lett.*, 1996, **76**, (17), 3168–3171.
74. E. Prodan and W. Kohn: *Proc. Natl. Acad. Sci. USA*, 2005, **102**, (33), 11635–11638.
75. W. Kohn: *Phys. Rev.*, 1959, **115**, (4), 809–821.
76. J. des Cloizeaux: *Phys. Rev.*, 1964, **135**, (3A), A698.
77. G. Nencieu: *Commun. Math. Phys.*, 1983, **91**, (1), 81–85.
78. L. He and D. Vanderbilt: *Phys. Rev. Lett.*, 2001, **86**, (23), 5341–5344.
79. S. Ismail-Beigi and T. A. Arias: *Phys. Rev. Lett.*, 1999, **82**, (10), 2127–2130.
80. M. C. Payne, M. Teter, D. C. Allan, T. A. Arias and J. D. Joannopoulos: *Rev. Mod. Phys.*, 1992, **64**, (4), 1045–1097.
81. R. McWeeny: *Rev. Mod. Phys.*, 1960, **32**, (2), 335–369.
82. E. Hernandez and M. J. Gillan: *Phys. Rev. B*, 1995, **51**, (15), 10157–10160.
83. C. K. Skylaris, A. A. Mostofi, D. Haynes, O. Dieguez and M. C. Payne: *Phys. Rev. B*, 2002, **66**, (7), 035119.
84. P. D. Haynes, C. K. Skylaris, A. A. Mostofi and M. C. Payne: *Chem. Phys. Lett.*, 2006, **422**, (4–6), 345–349.
85. A. Ruiz-Serrano, N. D. M. Hine and C. K. Skylaris: *J. Chem. Phys.*, 2012, **136**, (23), 234101.
86. K. Skylaris, D. Haynes, A. A. Mostofi and M. C. Payne: *J. Phys.*, 2005, **17**, (37), 5757–5769.
87. L. E. Ratcliff, N. D. M. Hine and D. Haynes: *Phys. Rev. B.*, 2011, **84**, (16), 165131.
88. T. J. Zuehlsdorff, N. D. M. Hine, J. S. Spencer, N. M. Harrison, D. J. Riley and D. Haynes: *J. Chem. Phys.*, 2013, **139**, (6), 064104.
89. J. Perdew, K. Burke and M. Ernzerhof: *Phys. Rev. Lett.*, 1996, **77**, (18), 3865–3868.
90. X. Gonze, R. Stumpf and M. Scheffler: *Phys. Rev. B*, 1991, **44**, (16), 8503–8513.
91. Available at: http://opium.sourceforge.net/sci.html
92. B. G. Pfrommer, M. Côté, S. G. Louie and M. L. Cohen: *J. Comput. Phys.*, 1997, **131**, (1), 233–240.
93. K. A. Wilkinson, N. D. M. Hine and C. K. Skylaris: *J. Chem. Theory Comput.*, 2014, **10**, (11), 4782–4794.
94. Available at: http://ark.intel.com/products/75283/Intel-Xeon-Processor-E5-2697-v2-30M-Cache-2_70-GHz
95. J. Bernholc, E. L. Briggs, D. J. Sullivan, C. J. Brabec, M. B. Nardelli, K. Rapcewicz, C. Roland and M. Wensell: *Int. J. Quantum Chem.*, 1997, **65**, (5), 531–543.
96. E. Artacho, E. Anglada, O. Dieguez, J. D. Gale, A. Garcia, J. Junquera, R. M. Martin, J. M. Ordejon, D. Pruneda, D. Sanchez-Portal and J. M. Soler: *J. Phys*, 2008, **20**, (3), 064208.
97. C. K. Skylaris and D. Haynes: *J. Chem. Phys.*, 2007, **127**, (16), 164712.
98. J. D. Elliott, N. D. M. Hine, A. A. Mostofi, G. Teobaldi: [to be submitted]
99. N. D. M. Hine, W. Avraam, P. Tangney and D. Haynes: *J. Phys.*, 2012, **367**, 012002.
100. E. Poli, J. D. Elliott, N. D. M. Hine, A. A. Mostofi, G. [to be submitted] Teobaldi